JOURNAL OF GEOPHYSICAL RESEARCH, VOL. 103, NO. C9, PAGES 18,839-18,849, AUGUST 15, 1998

Imaging of ocean waves on both sides of an atmospheric front by the SIR-C/X-SAR multifrequency synthetic aperture radar

Christian Melsheimer, Mingquan Bao[1], and Werner Alpers
Institut für Meereskunde, Universität Hamburg, Hamburg, Germany

Abstract. Radar images of an ocean scene containing an atmospheric front and almost range-propagating ocean waves which were acquired by the multifrequency/multipolarization synthetic aperture radar (SAR) aboard the space shuttle *Endeavour* during the spaceborne imaging radar-C/X-band synthetic aperture radar (SIR-C/X-SAR) mission over the North Atlantic in 1994 are analyzed. The L-band SAR image spectra calculated from two areas located on opposite sides of the atmospheric front are quite similar, whereas the corresponding X- and C-band SAR image spectra differ significantly. It is shown that this is a consequence of the SAR imaging mechanism; at L band the SAR imaging mechanism depends weakly on the local wind field, and at X and C band it depends strongly on the local wind field. This is in agreement with earlier results obtained from the analysis of airborne multifrequency/multipolarization SAR images acquired over the North Sea during the SAR and X-Band Ocean Nonlinearities - Forschungsplattform Nordsee (SAXON-FPN) experiment. In this investigation it was found that at X and C band the phase of the real aperture radar modulation transfer function (RAR MTF) changes by almost 90°, when in the reference system moving with the group velocity of the dominant wave, the component of the wind velocity in the direction of the wave propagation changes sign. However, at L band such a change in local wind direction affects the phase of the RAR MTF only slightly. Using this phase behavior of the RAR MTF in simulations of the SIR-C/X-SAR image spectra, we show that the observed differences of the X- and C-band SAR image spectra measured on both sides of the atmospheric front are consistent with a change in wind speed and direction across the front. From this we conclude that for inverting X- or C-band SAR image spectra into ocean wave spectra that contain ocean waves propagating near the range direction, it is quite important to have a good knowledge of the local wind field, whereas for L-band SAR image spectra this is of minor importance.

1. Introduction

It is well known that synthetic aperture radar (SAR) imagery acquired over the ocean can be used to obtain information on the two-dimensional ocean wave spectrum. However, the inversion of SAR image spectra into ocean wave spectra can be quite intricate. First, one has to cope with the often occurring nonlinearity in the SAR imaging mechanism of ocean waves which results from the motion of the ocean surface, and second, one has to cope with the ocean wave-radar modulation transfer function whose value, in general, is not well known. This modulation transfer function describes the modulation of the normalized radar cross section (NRCS) by the long ocean waves. It is often also called real aperture radar modulation transfer function (RAR MTF) because it relates ocean wave spectra to real aperture radar (RAR) image spectra [*Brüning et al.*, 1994]. In the case of SAR imaging of ocean waves which propagate near the range (across-track) direction this RAR MTF contributes significantly to the SAR imaging mechanism.

The RAR MTF consists of three parts: the tilt, the range bunching, and the hydrodynamic MTF as described, e.g., in the papers by *Hara and Plant* [1994] and *Brüning et al.* [1994]. Most authors assume that the first two MTFs are well known and that they can be calculated by using Bragg scattering theory in con-

[1]now at Centre for Remote Imaging, Sensing and Processing (CRISP), Faculty of Science, National University of Singapore, Singapore.

Paper number 98JC00457.
0148-0227/98/98JC-00457$09.00

junction with the composite surface model. However, the hydrodynamic MTF is less well known; there is ample experimental evidence that the usually applied weak hydrodynamical interaction theory cannot fully explain the measured values of the hydrodynamic MTF [*Alpers et al.*, 1981, *Brüning et al.*, 1994]. It seems that wave-induced wind stress modulation plays a major role in the modulation of the NRCS by the long ocean waves [*Romeiser et al.*, 1994; *Kudryavtsev et al.*, 1997]. Previously, the hydrodynamic MTF has been determined experimentally from radar backscatter measurements carried out from sea-based platforms [*Plant et al.*, 1983; *Schröter et al.*, 1986; *Feindt et al.*, 1986; *Schmidt et al.*, 1995] and from comparisons of measured and simulated SAR image spectra [*Brüning et al.*, 1994; *Jacobsen and Høgda*, 1994]. The hydrodynamic MTF has also been estimated by comparing significant wave heights calculated by a wave prediction model with wave heights inverted from SAR data by using the phase of the hydrodynamic MTF as a fitting parameter [*Monaldo et al.*, 1993].

The presently applied scheme for inverting the SAR image spectra calculated from images acquired by the C-band SAR aboard the first and second European Remote Sensing satellites (ERS-1, ERS-2) is based on the assumption that the RAR MTF is dominated by the tilt MTF, because the radars aboard these two satellites operate at steep incidence angles (around 23°), where theory predicts that the tilt MTF is large. Thus it is argued that the exact knowledge of the hydrodynamic MTF is not required for the inversion of these ERS SAR image spectra into ocean wave spectra [*Hasselmann et al.*, 1996]. However, at intermediate incidence angles we expect that most of the time the hydrodynamic MTF is larger than the sum of the tilt and range bunching MTFs. Therefore, at these incidence angles, the hydrodynamic MTF plays an important role in the SAR imaging of ocean waves, in particular, of those waves that propagate near the range direction. The SAR flown aboard the space shuttle *Endeavour* during the spaceborne imaging radar-C/X-band SAR (SIR-C/X-SAR) missions in April and October 1994 operated frequently at intermediate incidence angles, and thus the SAR images acquired during this mission are particularly suited for studying the effect of the hydrodynamic modulation on the SAR imaging mechanism of ocean waves. The SIR-C/X-SAR data set acquired over the ocean allows one to study the SAR imaging mechanism of ocean waves as a function of radar frequency and polarization. The SIR-C/X-SAR radar system operated at frequencies of 1.25 GHz (L band), 5.3 GHz (C band), and 9.6 GHz (X band). At L and C band it could transmit and receive at horizontal (H) and vertical (V) polarization and thus had the capability to make measurements at the polarization combinations HH, VV, HV, and VH. At X band, only vertically polarized microwaves could be transmitted and received. The ocean scene in the North Atlantic analyzed in this investigation was imaged at VV polarization and at all three radar frequencies (mode 9 in the SIR-C/X-SAR nomenclature). The incidence angle at the center of the SAR swath was 51.3°.

The present study in which SIR-C/X-SAR images containing ocean waves located on both sides of an atmospheric front are analyzed confirms previous findings that at X and C band the hydrodynamic MTF depends strongly on wind speed and direction, whereas at L band it depends only weakly on them [*Plant et al.*, 1983; *Brüning et al.*, 1994; *Zurk and Plant*, 1996]. Ocean scenes containing atmospheric fronts are particularly suited for such studies because the wind direction changes abruptly across such fronts. *Jacobsen and Høgda* [1994] have already studied the SAR imaging of ocean waves on both sides of an atmospheric front, but their investigation was confined to one radar frequency (C band) only. By using Monte Carlo simulations we show in this investigation that the measured SAR image spectra can be reproduced fairly well when taking into account the previously found dependence of the RAR MTF on the local wind speed and direction in the SAR imaging mechanism [*Brüning et al.*, 1994; *Jacobsen and Høgda*, 1994; *Zurk and Plant*, 1996]. This investigation corroborates previous findings obtained from the analysis of multifrequency/multipolarization airborne SAR imagery that for ocean waves propagating near the range direction, the local wind strongly affects the SAR imaging mechanism at X and C band but only weakly at L band.

2. SIR-C/X-SAR images and spectra

Figure 1 shows X-, C-, and L-band, VV polarization, SAR images of an ocean scene in the North Atlantic in the vicinity of the North Atlantic Ridge at 49.2°N, 31.0°W, covering an area of 47.7 × 12.6 km. These three SAR images were acquired simultaneously from the space shuttle *Endeavour* during the first SIR-C/X-SAR flight on April 15, 1994, at 0754:58 UTC (data take 96.3). The flight direction of the space shuttle (from left to right in the image) was toward 60.3° relative to north (using the convention that the angle is positive to the east). The antenna was looking to the right-hand side of the flight direction, and the incidence angle θ in the center of this SAR swath was θ=51.3°. All SAR images have a spatial resolution of 25 m in range as well as in azimuth direction (four-look averages in azimuth direction).

One remarkable feature visible on these SAR images is the irregularly shaped dark band in their center, which is particularly pronounced in the X- and C-band SAR images, and which, in geographical coordinates, is aligned approximately in the direction from 10° relative to north to 190° relative to north. Inspection of the meteorological surface map of April 15, 1994, at 0600 UTC, which is reproduced in Figure 2, reveals that an atmospheric front crosses the imaged area and that it has the same orientation as the dark band in the SAR images. On this map the atmospheric front is marked as a cold front which is moving eastward and which is accompanied by rain. We therefore interpret the dark band,

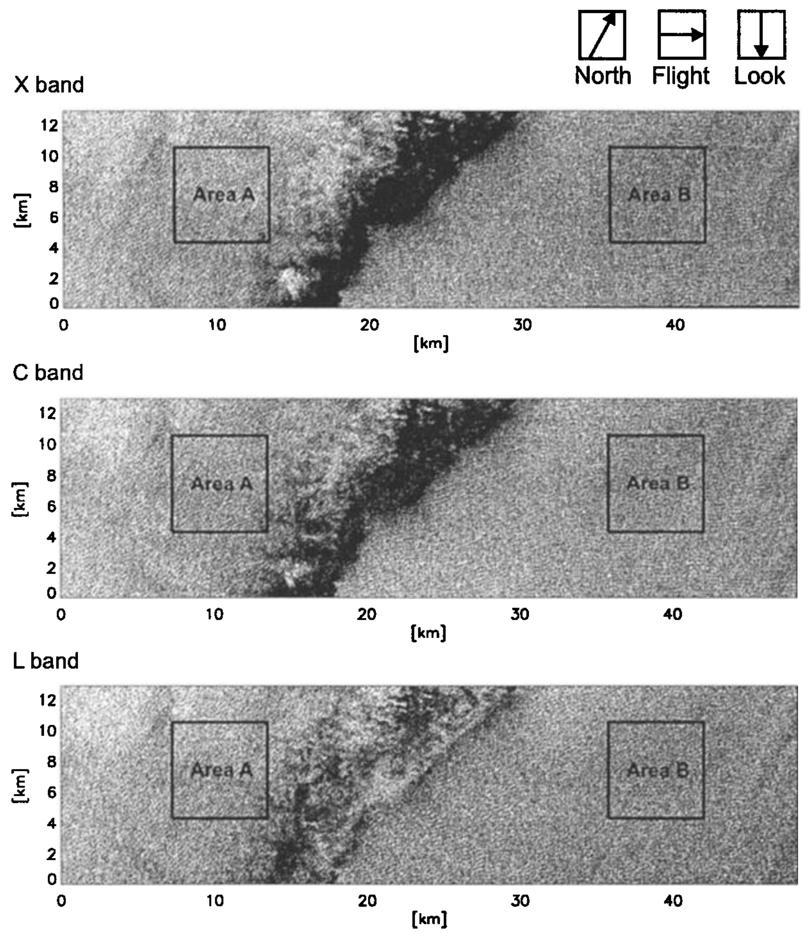

Figure 1. X-band, C-band, and L-band, VV polarization, SIR-C/X-SAR images of an ocean area in the North Atlantic acquired on April 15, 1994, at 0754:58 UTC from the space shuttle *Endeavour*. The dark band in the center originates from an atmospheric front.

which is an area of strongly reduced radar backscattering, as the sea surface manifestation of the atmospheric front. We conjecture that it is caused by sea surface roughness variations induced mainly by raindrops impinging on the sea surface, generating turbulences in the upper water layer, and thus attenuating the Bragg waves. At X band and, to a lesser extent, also at C band the scattering and attenuation of the microwaves by raindrops in the atmosphere may also contribute to the radar signature of the atmospheric front, but we expect these contributions to be small in this case [*Melsheimer et al.*, this issue]. Visual inspection of these SAR images of Figure 1 reveals that the atmospheric front is imaged quite similarly at X and C band but differently at L-band. On all three SAR images, ocean waves can be delineated on both sides of the atmospheric front. However, most strikingly, in the X- and C-band images the waves on both sides of the front seem to propagate in quite different directions, whereas in the L-band image they seem to propagate almost in the same direction. In the X- and C-band images, on the right-hand side of the front (area B), the ocean waves seem to propagate approximately in range direction, whereas on the left-hand side of the front (area A) they seem to propagate approximately at an angle of 30° off the range direction. In order to quantify this we have calculated the X-, C-, and L-band SAR image spectra on both sides of the atmospheric front and have plotted them in Figure 3. In these plots, k_x and k_y are the wavenumbers in flight

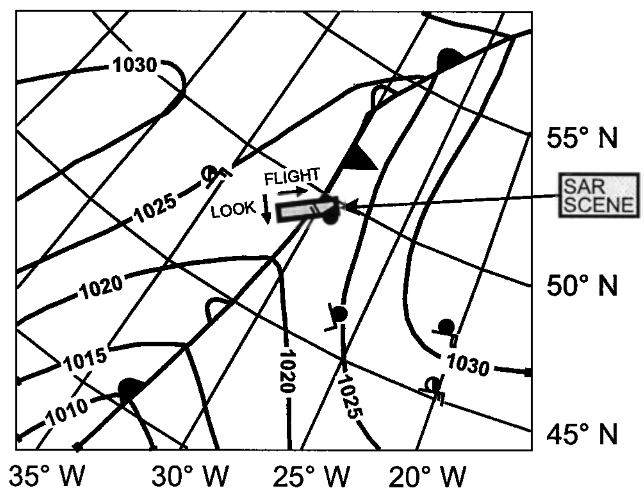

Figure 2. Meteorological surface map of a section of the North Atlantic on April 15, 1994, 0600 UTC. The imaged ocean area shown in Figure 1 is indicated by a grey box.

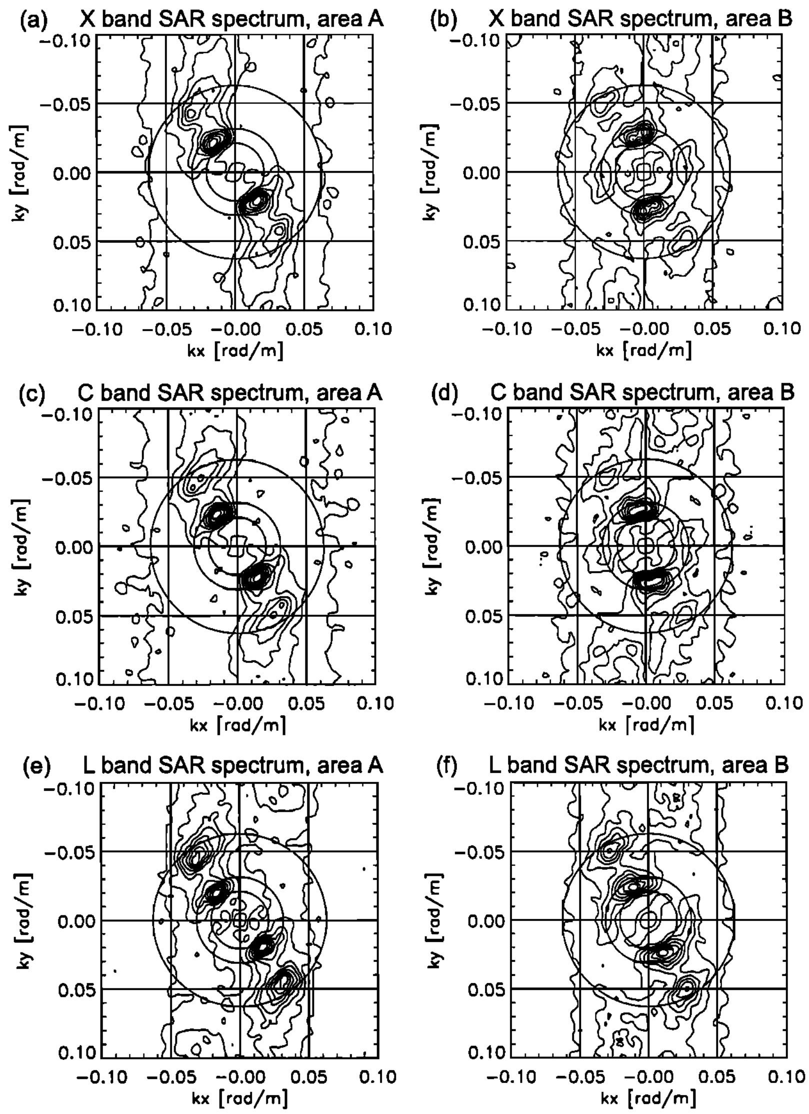

Figure 3. Measured SAR image spectra calculated from the areas A and B marked in Figure 1. (a, b) X-band, (c, d) C-band, and (e, f) L-band SAR image spectra. Figures 3a, 3c, and 3e are from area A, and Figures 3b, 3d, and 3f are area B. The wavenumber in flight direction is k_x, the wavenumber in ground range direction is k_y. Inserted in all plots are three circles on which the wavelength is 300, 200, and 100 m (from the center outward).

(azimuth) direction and ground range direction, respectively. The positive k_x axis points in azimuth direction (i.e., to the right in the plots), and the positive k_y axis points in ground range direction (i.e., downward in the plots). Thus we are dealing here with a left-handed coordinate system. The azimuth angle is defined in such a way that it is zero in azimuth (flight) direction and positive to the right-hand side of this direction. Figures 3a and 3b show the X-band, Figures 3c and 3d show the C-band, and Figures 3e and 3f show the L-band SAR image spectra. The spectra on the left-hand side are from area A, while the spectra on the right-hand side are from area B (see Figure 1). The centers of both areas are separated by about 25.6 km. The SAR image spectra shown in Figure 3 are normalized by the spectral energy density at the highest peak and are plotted in a linear scale with isoline spacing of 0.1. The three circles inserted in the plots mark the wavelengths of 300 m (inner circle), 200 m (middle circle), and 100 m (outer circle). The SAR image spectra shown in Figure 3 are calculated from nine subimages, each consisting of 256 × 256 pixels (pixel size is 12.5 × 12.5 m). First, two-dimensional Fourier transforms of all subimages are calculated, then they are squared, averaged, and smoothed by averaging over 3 by 3 spectral grid points using a triangle filter. Furthermore, the spectral clutter noise floor is subtracted from the SAR spectrum by using the method described by *Brüning et al.* [1994].

On all SAR image spectra plotted in Figure 3, two ocean wave systems can be delineated. The wavelengths of the spectral peaks vary slightly from spectrum to spectrum. For example, at X band, area A (Figure 3a), one spectral peak is located at 236 m and the other at 112 m, while at X band, area B (Figure 3b), they

Table 1. Wavelength and Direction at Which the two Spectral Peaks in the Six Measured SAR Image Spectra Shown in Figure 3 Are Located

	Area A				Area B				
Band	$\lambda_p^{(1)}$, m	$\lambda_p^{(2)}$, m	$\Phi_p^{(1)}$, deg	$\Phi_p^{(2)}$, deg	$\lambda_p^{(1)}$, m	$\lambda_p^{(2)}$, m	$\Phi_p^{(1)}$, deg	$\Phi_p^{(2)}$, deg	$\Phi_p^{(1)}$ (B) − $\Phi_p^{(1)}$ (A), deg
X	236	112	57	53	223	105	90	59	33
C	223	112	55	57	223	105	76	60	21
L	236	112	53	55	223	105	66	60	13

Here λ_p is the wavelength, and Φ_p is the direction. The direction is measured relative to the flight (azimuth) direction. The superscripts (1) and (2) refer to the spectral peaks in the SAR image spectra associated with the primary and the secondary wave systems, respectively.

are located at 223 and 105 m, respectively. Noticeable is that the wave system with the spectral peak at the higher wavenumber (secondary wave system) is imaged better at L band than at X band; that is, the spectral energy densities associated with the high-wavenumber wave system are larger at L band than at X band. Furthermore, this high-wavenumber wave system is imaged slightly better in area B than in area A.

However, the most striking observation in these plots is that at X band the spectral peak of the low wavenumber wave system (primary wave system) is rotated in area B by 33° relative to area A (in clockwise direction). At C band the rotation angle is 21°, and at L band it is 13°. The wavelengths and directions (relative to the flight direction) at which the two spectral peaks in all six SAR images plotted in Figure 3 are located are summarized in Table 1.

From the oceanography of the North Atlantic we know that at this part of the North Atlantic, no strong gradients of the surface current field exist. Therefore we can state that such large rotations of spectral peaks on both sides of the atmospheric front as observed in the X- and C-band SAR images cannot be attributed to wave-current interactions. Another argument that the apparently different propagation directions of the long wave system on both sides of the atmospheric front seen in the X- and C-band SAR images cannot be dynamically induced is that in the L-band SAR image both propagation directions are almost equal. We therefore conjecture that this rotation in the SAR image is caused by the SAR imaging mechanism. Indeed, we shall show in section 3 that this rotation is an artifact of the SAR imaging mechanism and that this is consistent with earlier results obtained from the analysis of SAR data acquired over the North Sea by a multifrequency/multipolarization airborne SAR during the SAR and X-Band Ocean Nonlinearities – Forschungsplattform Nordsee (SAXON-FPN) experiment [*Brüning et al.*, 1994].

3. SAR Imaging Mechanism

In order to demonstrate that the observed differences in the SAR image spectra at both sides of an atmospheric front are artifacts of the SAR imaging mechanism, we first show by Monte Carlo simulations with a model ocean wave spectrum how the phase of the RAR MTF affects the rotation of the spectral peak in the SAR image spectrum (section 3.1). Then we give a physical explanation for this rotation by using the quasi-linear transform (section 3.2). Finally, we carry out Monte Carlo simulations for the scenes on both sides of the atmospheric front imaged by SIR-C/X-SAR (section 3.3).

3.1. Monte Carlo Simulations With a Model Ocean Wave Spectrum

In this section we present three SAR image spectra that have been calculated from a model ocean wave spectrum (Figure 4a) by using three different values of the phase of the RAR MTF, η_0^{RAR}, in the SAR imaging mechanism. These calculations have been carried out by using Monte Carlo simulation techniques as described, e.g., by *Brüning et al.* [1990, 1994]. The underlying SAR imaging theory is the velocity bunching theory, which also incorporates the modulation of the NRCS by the long ocean waves. This modulation is described by the dimensionless RAR MTF, $M^{\mathrm{RAR}}(\mathbf{k})$. In the simulations presented in this section we have approximated $M^{\mathrm{RAR}}(\mathbf{k})$ by

$$\begin{aligned} M^{\mathrm{RAR}}(\mathbf{k}) &= 0.5|M_0^{\mathrm{RAR}}|(1+\sin^2\Phi) \\ &\quad \cdot \exp\left[-i\eta_0^{\mathrm{RAR}}\mathrm{sign}(k_y)\right] \end{aligned} \tag{1}$$

and have chosen the following values: $|M_0^{\mathrm{RAR}}| = 10$ and $\eta_0^{\mathrm{RAR}} = 0°, 45°, 90°$. Here Φ denotes the azimuth angle of the ocean wave propagation direction (the range direction corresponds to $\Phi = 90°$), and $\mathrm{sign}(k_y)$ denotes the sign of k_y [see also *Brüning et al.*, 1994]. As input spectrum for the simulations, we have used a Joint North Sea Wave Atmosphere Program (JONSWAP) spectrum where the dominant wave propagates in range direction ($\Phi_p = 90°$). The dominant wavelength is $\lambda_p = 200$ m, the significant wave height is $H_s = 3$ m, and the wind speed (at a height of 10 m) is 20 m/s. The radar parameters used in these simulations are the incidence angle $\theta = 51.3°$ and the ratio $R/V = 46$ s, where R denotes the range of the target and V denotes the platform velocity. The resulting sim-

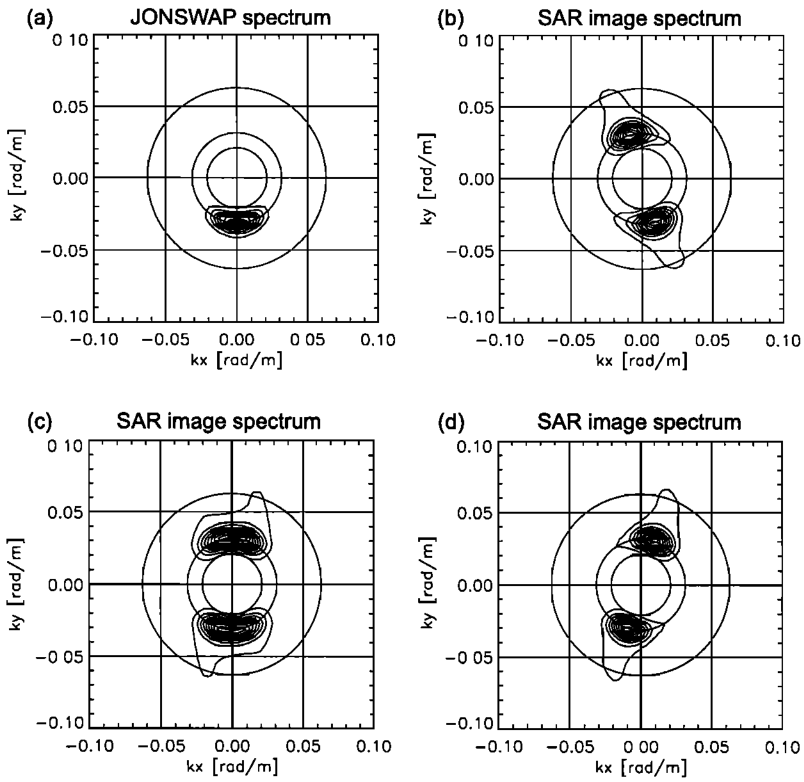

Figure 4. (a) Joint North Sea Wave Atmospheric Program (JONSWAP) spectrum. Ocean wave spectra calculated from this JONSWAP spectrum by Monte Carlo simulations with different real aperture radar modulation transfer function (RAR MTF) phases: η_0^{RAR} = (b) 0°, (c) 45°, and (d) 90°.

ulated SAR image spectra are plotted in Figures 4b, 4c, and 4d. We see that the spectral peak is rotated in different directions depending on the value of the phase of the RAR MTF, η_0^{RAR}.

3.2. Quasi-linear Transform

In this section we show that the reason for the rotation of the SAR image spectra is an interference between the phase of the RAR MTF and the velocity bunching MTF defined below. This can be shown best by using the quasi-linear transform. The quasi-linear transform is an approximation of the SAR imaging mechanism of ocean waves which is applicable when the degree of nonlinearity of the SAR imaging mechanism is small (typically < 0.5). The parameter that describes the degree of nonlinearity is defined by [*Alpers*, 1983; *Brüning et al.*, 1990]

$$c = \frac{R}{4V} g^{1/2} k_p^{3/2} H_s |\cos \Phi_p| \tag{2}$$

where $k_p = 2\pi/\lambda_p$ is the wavenumber of the dominant wave, Φ_p is the angle between the flight (azimuth) direction and the propagation direction of the dominant wave, H_s is the significant wave height, and g is the acceleration of gravity. We note that the nonlinearity parameter vanishes for range-traveling waves ($\Phi_p = 0$). Thus, for waves traveling sufficiently close to the range direction, the quasi-linear transform is applicable. The quasi-linear transform relates the ocean wave spectrum, $P_o(\mathbf{k})$, to the SAR image spectrum, $P_s(\mathbf{k})$, by the following equation [*Hasselmann and Hasselmann*, 1991]

$$\begin{aligned} P_s(\mathbf{k}) &= \exp\left(-k_x^2 \frac{R^2}{V^2}\sigma^2\right) |\mathbf{k}|^2 \\ &\cdot \left[|M^{\mathrm{SAR}}(\mathbf{k})|^2 \frac{P_o(\mathbf{k})}{2} + |M^{\mathrm{SAR}}(-\mathbf{k})|^2 \frac{P_o(-\mathbf{k})}{2} \right] \end{aligned} \tag{3}$$

Here σ^2 denotes the variance of the orbital velocity of the Bragg scattering elements (facets), and M^{SAR} denotes the total (nondimensional) SAR MTF, which consists of the sum of the (nondimensional) RAR MTF, M^{RAR}, and the (nondimensional) velocity bunching MTF, M^{vb} [*Brüning et al.*, 1990]

$$M^{\mathrm{SAR}} = M^{\mathrm{RAR}} + M^{vb} \tag{4}$$

where M^{RAR} is given by (1) and M^{vb} is given by [*Brüning et al.*, 1994]

$$\begin{aligned} M^{vb}(\mathbf{k}) &= |M^{vb}| \exp(-i\eta^{vb}) \\ &= -\frac{R}{V}\Omega \cos\Phi \{\cos\theta - i \sin\Phi \sin\theta\} \end{aligned} \tag{5}$$

Here $\Omega = \sqrt{g|\mathbf{k}|}$ denotes the angular frequency of the

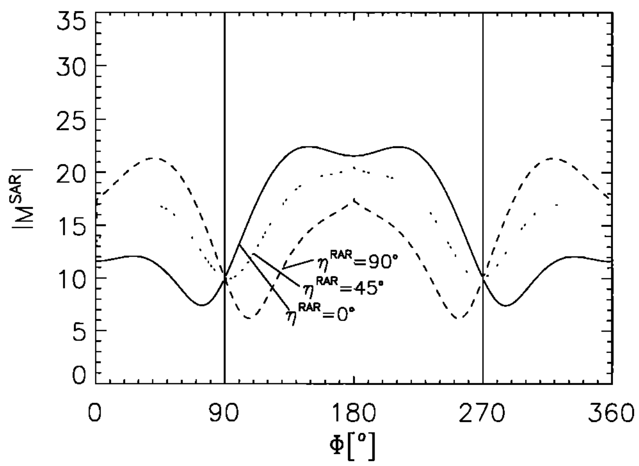

Figure 5. Modulus of the quasi-linear SAR MTF versus the azimuth angle, Φ, of the ocean wave propagation direction for three different phases of the RAR MTF: $\eta_0^{RAR} = 0°$ (solid), 45°(dotted), and 90° (dashed). The angle Φ is zero in flight direction and 90° in range direction.

ocean wave with wavenumber $|\mathbf{k}|$. Note that the $\mathbf{k}$ dependence of $M^{vb}(\mathbf{k})$ is implicit in Φ since $\tan\Phi = k_y/k_x$. From (1), (4), and (5) we obtain the following expression for the squared modulus of the SAR MTF

$$|M^{SAR}|^2 = |M^{RAR}|^2 + |M^{vb}|^2 + 2|M^{RAR}||M^{vb}|\cos(\eta^{RAR} - \eta^{vb}) \quad (6)$$

The dependence of the modulus of the SAR MTF on the azimuth angle, Φ, at constant wavenumber, $|\mathbf{k}|$, for three different phases of the RAR MTF, $\eta_0^{RAR} = 0°$, $\eta_0^{RAR} = 45°$, and $\eta_0^{RAR} = 90°$, is shown in Figure 5. In this example we have used the following values, which are consistent to the SIR-C/X-SAR scene presented in section 2 and to the simulations in section 3.1: $R/V = 46$ s, $\theta = 51.3°$, $\lambda_p = 200$ m (i.e., $|\mathbf{k}_p| = 2\pi/200$ m^{-1}), and $|M_0^{RAR}| = 10$. Figure 5 clearly shows that the modulus of the SAR MTF has a minimum near range direction ($\Phi = 90°$) and that the exact location of this minimum varies with the phase of the RAR MTF, η_0^{RAR}.

If we assume that the ocean wave spectrum is zero in one half of the wavenumber plane (e.g., considering a unimodal spectrum) i.e., $P_o(\mathbf{k}) = 0$ for $k_y < 0$, then the SAR image spectrum in the half plane $k_y > 0$ is, according to (3), proportional to the product of $|M^{SAR}(\mathbf{k})|^2$ and $P_o(\mathbf{k})$

$$P_s(\mathbf{k}) \propto |M^{SAR}(\mathbf{k})|^2 P_o(\mathbf{k}) \quad (7)$$

(This determines also $P_s(\mathbf{k})$ in the other half plane, since $P_s(-\mathbf{k}) = P_s(\mathbf{k})$, resulting from the invariance of (3) under the transform $\mathbf{k} \rightarrow -\mathbf{k}$.) On the basis of (7) and the plot of $|M^{SAR}|$ shown in Figure 5, we can readily explain why the phase of the RAR MTF, η_0^{RAR}, has such a strong effect in the SAR imaging of ocean waves propagating near the range direction. For these waves the spectral energy density of the ocean wave spectrum, $P_o(\mathbf{k})$, is concentrated near the positive k_y axis ($\Phi = 90°$). If $\eta_0^{RAR} = 90°$, then the product of $|M^{SAR}|^2$ with $P_o(\mathbf{k})$ yields the result that the spectral energy density of the SAR image spectrum is reduced at $\Phi > 90°$ (where $|M^{SAR}|$ has a minimum, see Figure 5, dashed line) and enhanced at $\Phi < 90°$. If, on the other hand, $\eta_0^{RAR} = 0°$, then the spectral energy density of the SAR image spectrum is enhanced at $\Phi > 90°$ and reduced at $\Phi < 90°$ (where $|M^{SAR}|$ has a minimum, see Figure 5, solid line). In the first case ($\eta_0^{RAR} = 90°$) the spectral peak is shifted toward smaller Φ; that is, it is rotated in anticlockwise direction. In the second case ($\eta_0^{RAR} = 0°$) it is rotated in clockwise direction. We shall show in the next section that at X and C band such a change of η_0^{RAR} (from $\eta_0^{RAR} = 0°$ to $\eta_0^{RAR} = 90°$) across the atmospheric front explains qualitatively the different SAR image spectra on both sides of the front.

The angle by which a peak of the SAR image spectrum is rotated also depends on the angular width (spreading) of the ocean wave spectrum $P_o(\mathbf{k})$; the peak of the resulting SAR image spectrum, $P_s(\mathbf{k})$, cannot lie outside the domain where the spectral energy of $P_o(\mathbf{k})$ is located, since $P_s(\mathbf{k})$ is proportional to $P_o(\mathbf{k})$ (see (7)). Moreover, if the peak of the ocean wave spectrum is not near range direction, the position of the corresponding peak of the SAR image spectrum is not influenced by the phase of the RAR MTF.

3.3. Monte Carlo Simulations for the SIR-C/X-SAR Scene

We now apply Monte Carlo simulations to the ocean scene imaged by SIR-C/X-SAR (Figures 1 and 3). Unfortunately, no simultaneous in situ measured oceanographic and meteorological data are available for the imaged scene. As for meteorological data, we only have the surface weather chart (Figure 2) at our disposal, which is too coarse to yield sufficiently accurate values of the local wind speed and direction at the location of the imaged scene. As for the oceanographic data, we can only recourse to hindcast ocean wave spectra provided by the European Centre for Medium-Range Weather Forecasts (ECMWF) at Reading, England. These spectra are calculated from wind fields by using the third generation wave prediction model WAM [*Wave Model Development and Implementation (WAMDI) Group*, 1988]. Figure 6a shows the WAM ocean wave spectrum for the position 49.0°N, 31.0°W on April 15, 1994, at 0800 UTC. This WAM spectrum lies closest in space and time to the imaged SAR scene, its position is about 25 km farther to the south, and the time lag is 7 min. In Figure 6 the ocean wave spectrum is plotted in the same coordinate system as the SAR image spectra shown in Figure 3. Like the SAR image spectra, it is normalized by the spectral energy density at the highest peak. Most of the spectrum is plotted with an isoline spacing of 0.1 (solid lines), but a part of it (in the upper section) is plotted with a finer spacing of 0.033 (dotted lines) in order to make visible also the weak secondary wave system.

We see from Figure 6a that the ocean wave field consists of three wave systems, which in the following we

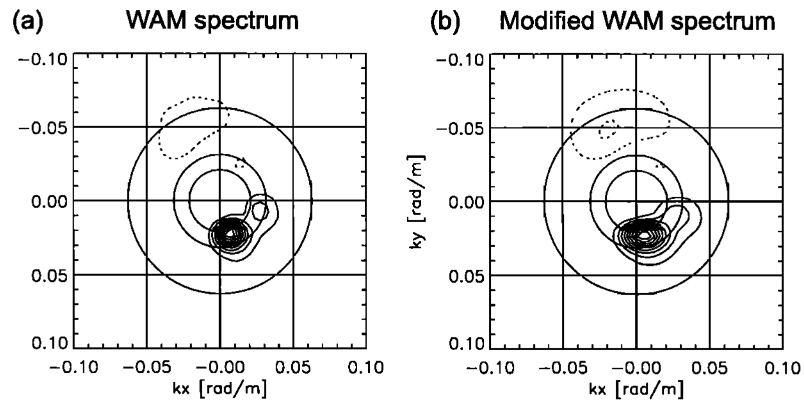

Figure 6. (a) Ocean wave spectrum calculated by the WAM model for the position 49.0°N, 31.0°W on April 15, 1994, at 0800 UTC. (b) "Best fit" ocean wave spectrum (modified WAM ocean wave spectrum) used in the SAR simulations as an input spectrum. The coordinate system is the same as that for the SAR image spectra of Figure 3.

shall call primary, secondary, and tertiary wave systems. The wavelengths and propagation directions (relative to the azimuth direction) of the dominant wave of the primary, secondary, and tertiary wave system are 250 m and 68°, 122 m and 254°, and 222 m and 15°, respectively (recall that in our convention the azimuth angle is positive to the right of the flight direction). According to the WAM the ocean waves have a significant wave height of 3.3 m.

Because of the lack of precise information on the input parameters for the Monte Carlo simulations we are unable to exactly reproduce the measured SIR-C/X-SAR spectra by simulations. In particular, with the hindcast WAM spectrum as input, we have been unable to simulate SAR image spectra that closely resemble the measured ones. From the discussion of the quasi-linear transform in section 3.2 we see that the imaging mechanism is only sensitive to the RAR MTF when the angular width (spreading) of the peak of the ocean wave spectrum is large enough and when the propagation direction of the dominant wave is close enough to range direction. Therefore, in order to obtain simulated SAR image spectra that closely resemble the measured ones, we have slightly modified the WAM ocean wave spectrum by rotating it toward the range direction by 5° and by broadening the spectrum in k_x direction (see Figure 6b). Note that the angle of rotation is smaller than the angular resolution of the original WAM ocean wave spectrum, which resides on a very coarse polar grid with only 25 frequency and 24 angular sectors with a width of 15°. Since our Monte Carlo simulations use a Cartesian wavenumber grid (129 × 129 grid points, $\Delta k = 0.0039$ m^{-1}), the WAM spectrum is also interpolated to this grid (which allows a much finer angular resolution than the original WAM spectrum) before being used as input to the simulations. Note also that the weak tertiary wave system visible in the unmodified WAM ocean wave spectrum (Figure 6a) has disappeared in the modified one (Figure 6b) because the filter has smeared out the peak associated with the tertiary wave system. However, this peak also does not show up in the measured SAR image spectra depicted in Figure 3, which is probably due to the small signal-to-noise ratio. We shall subsequently call the modified WAM ocean wave spectrum the "best fit" ocean wave spectrum.

Using this best fit spectrum (Figure 6b) as input to our Monte Carlo simulations, we only can achieve a reasonably good agreement between measured and simulated SAR spectra if we use the values of the RAR MTF listed in Table 2, which we may call best fit values. It turns out that for each wave system a separate RAR MTF has to be used. The SAR image spectra obtained from these Monte Carlo simulations are plotted in Figure 7. The wavelength ($\bar{\lambda}_p$) and direction ($\bar{\Phi}_p$) at which the two spectral peaks in the six simulated SAR image spectra are located are listed in Table 3. Comparing the measured and simulated SAR image spectra plotted in Figures 3 and 7, respectively, and comparing the wavelengths and directions of the spectral peaks of these spectra (see Tables 1 and 3), we see that the agreement is not perfect but that the basic features of the measured SAR image spectra are reproduced.

The simulations clearly show that in the X- and C-band SAR images the waves of the low-wavenumber

Table 2. Values of the Modulus and Phase of the (Nondimensional) RAR MTF Used in the Monte Carlo Simulations

	Area A		Area B	
Band	Modulus	Phase, deg	Modulus	Phase, deg
X	10	90*	15*	0
		0†	10†	
C	10	90*	15*	25*
		0†	10†	0†
L	10	90*	15*	55*
		0†	14†	0†

*Here $k \leq 0.04$ m^{-1}.
†Here $k > 0.04$ m^{-1}.

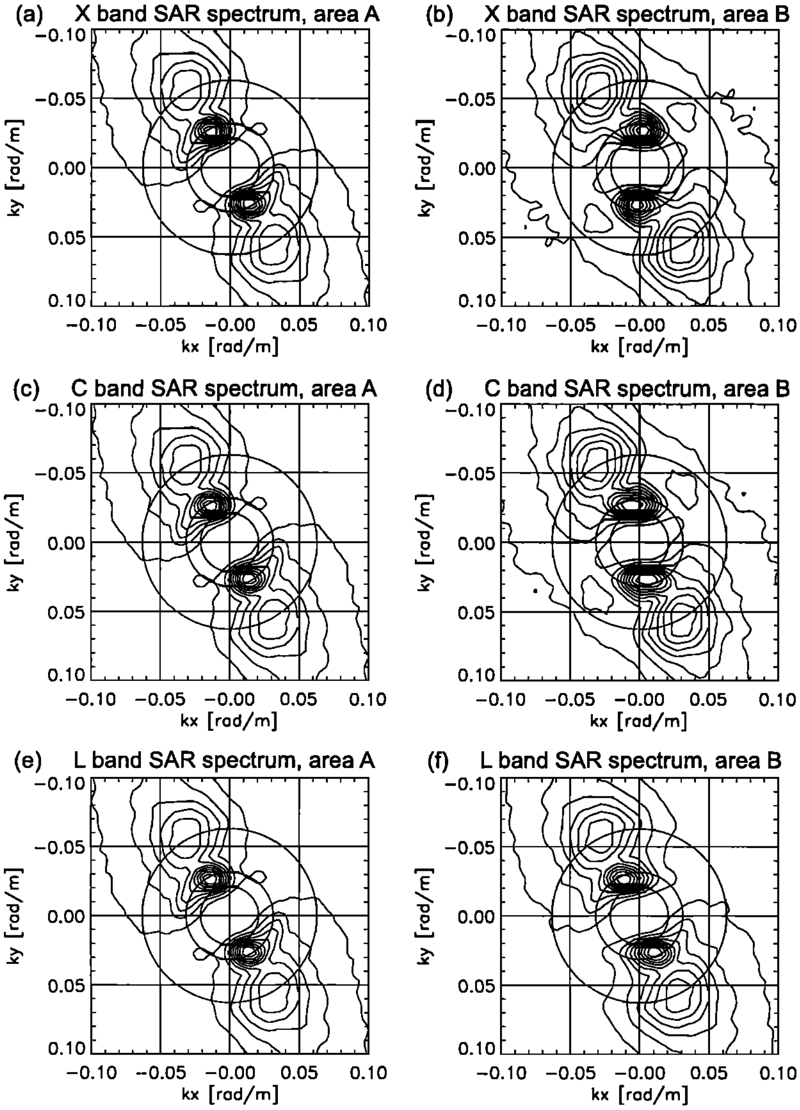

Figure 7. Simulated SAR image spectra for areas A and B. The ordering of the spectra and the annotation are the same as in Figure 3.

wave system propagate in quite different directions at both sides of the atmospheric front, which is in accordance with the observations. At X band the directional shifting of the primary wave system was measured to be 33°, whereas the simulations yield 32°. At C band the respective values are 21° (measured) and 15° (simulated), and at L band they are 13° (measured) and 5° (simulated). In the next section we shall discuss if the best fit values of the RAR MTFs listed in Table 2 are in agreement with previous results.

4. Discussion

The simulations show that the directional shifting of the primary wave system (wavelength >200 m) in the X- and C-band SAR image spectra can be explained by

Table 3. Wavelength and Direction at Which the Two Spectral Peaks in the Six Simulated SAR Image Spectra Shown in Figure 7 Are Located

	Area A				Area B				
Band	$\bar{\lambda}_p^{(1)}$, m	$\bar{\lambda}_p^{(2)}$, m	$\bar{\Phi}_p^{(1)}$, deg	$\bar{\Phi}_p^{(2)}$, deg	$\bar{\lambda}_p^{(1)}$, m	$\bar{\lambda}_p^{(2)}$, m	$\bar{\Phi}_p^{(1)}$, deg	$\bar{\Phi}_p^{(2)}$, deg	$\bar{\Phi}_p^{(1)}$ (B) - $\bar{\Phi}_p^{(1)}$ (A), deg
X	220	96	63	60	228	96	95	63	32
C	220	96	63	60	226	96	78	62	15
L	220	96	63	60	223	96	68	64	5

Here $\bar{\lambda}_p$ is the wavelength and $\bar{\Phi}_p$ is the direction. The notation is the same as in Table 1.

a large change of the phase of the RAR MTF (X band, 90°to 0°; C band, 90°to 25°) across the front. The fact that the secondary wave system (wavelength 100 m) experiences no directional shifting can be explained by keeping the phase of the RAR MTF equal to zero on both sides of the front. Furthermore, we know that there is a drastic change in wind direction and speed across the front.

We shall now investigate whether the phases of the RAR MTF used in the simulations are realistic. According to findings by *Brüning et al.* [1994], who have determined the RAR MTFs by comparing measured and simulated SAR image spectra, the phase of the X- and C-band RAR MTF strongly depends on the wind direction relative to the wave propagation direction. This is probably caused by the modulation of the wind stress by the (long) ocean waves [*Romeiser et al.*, 1994; *Kudryavtsev et al.*, 1997]. According to *Brüning et al.* [1994] the dependence of the RAR MTF phase on the wind direction relative to the wave propagation direction can be expressed by introducing the parameter β defined by

$$\beta = \frac{U \cos\varphi - c_{gr}}{c_{gr}} \qquad (8)$$

Here U denotes the wind velocity, φ denotes the angle between the wave propagation direction and the direction into which the wind is blowing, and c_{gr} denotes the group velocity of the dominant wave in the wave system. If, in the reference system moving with the group velocity of the dominant wave, the wind has a component that blows in wave propagation direction (i.e., $U \cos\varphi > c_{gr}$), then $\beta > 0$. On the other hand, if, in the reference system moving with the group velocity of the dominant wave, the wind has a component that blows against the wave propagation direction (i.e., $U \cos\varphi < c_{gr}$), then $\beta < 0$. *Brüning et al.* [1994] found that the phase of the X-band RAR MTF is close to 90° for $\beta > 0$ and close to 0° for $\beta < 0$. At C band the phase of the RAR MTF lies between 60° and 90° for $\beta > 0$ and between 0° and 35° for $\beta < 0$. At L band they found no distinct dependence of the phase of the RAR MTF on the sign of β. This phase fluctuates between 15° and 90°, independent of the sign of β. One implication of this is that each wave system in a multimodal ocean wave spectrum has to be assigned its own RAR MTF, since wave systems with different propagation directions and group velocities can have different β values.

It is thus indeed possible that a wind shift causes a change of the sign of β for one wave system and hence a large shift of η_0^{RAR} for X and C band, while leaving the value of β and hence η_0^{RAR} unchanged for another wave system. The simplest scenario for this phenomenon consists of two wave systems having the same group velocity, but propagating in opposite directions, and wind blowing in the propagation direction of one of the wave systems (i.e., $\varphi_1 = 0°$ and $\varphi_2 = 180°$) with a wind speed U larger than the group velocity c_{gr} of the wave systems. Then the parameter β is positive [$\beta = (U - c_{gr})/c_{gr}$] for one wave system and negative [$\beta = -(U + c_{gr})/c_{gr}$] for the other. A shift of the wind direction by only 90°(such that $\varphi_1 = \varphi_2 = 90°$) results in negative β ($\beta = -1$) for both wave systems.

The case presented in this paper is not ideal, since the calculation of the β values suffers from the lack of exact in situ data about the wind. In the weather chart (Figure 2) the kink in the isobars at the atmospheric front indicates that the direction into which the wind was blowing changed drastically across this front, from 210° (±20°) with respect to north in area A to 340° (±20°) with respect to north in area B. Using these wind directions, the average values of the NRCS in areas A and B of the C-band SAR image (Figure 1, middle) can be converted into wind speeds by applying the CMOD4 wind scatterometer model [*Stoffelen and Anderson*, 1997]. With this model we obtain the following wind speed estimates: 17.5 m/s in area A and 9.3 m/s in area B, with error bars of about 3 m/s owing to the errors in the wind direction derived from the meteorological surface map and owing to uncertainties in the CMOD4 model. The wind directions in areas A and B as well as the propagation directions of the primary and secondary wave systems in the best fit ocean wave spectrum (modified WAM spectrum) are depicted in Figure 8. The group velocities of the primary and secondary wave systems are c_{gr} = 6.9 m/s and c_{gr} = 9.8 m/s.

Because of the sensitivity of β to the values of wind speed and direction within the error bars, the best fit values of the phase of the RAR MTF cannot unambiguously be inferred from the available wind data. We can only state that within the error bars of wind speed and direction we may infer that for the primary wave system

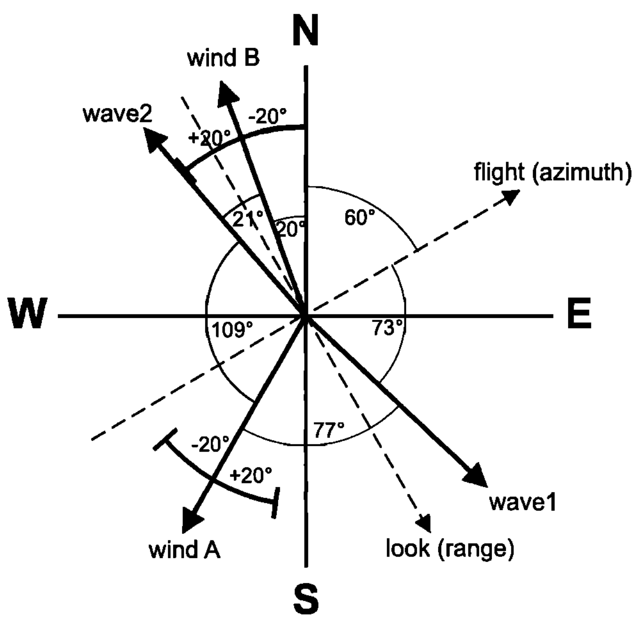

Figure 8. Diagram showing the propagation directions of the primary and secondary wave system of the modified WAM spectrum ("wave1" and "wave2," respectively) and the wind directions in areas A and B as inferred from the weather chart ("wind A" and "wind B," respectively). Note that here the wind direction denotes the direction into which the wind is blowing.

the β value has changed sign across the front, whereas for the secondary wave system it has not changed sign. This implies that the primary wave system is rotated in the X- and C-band SAR images but not the secondary wave system.

5. Conclusions

The case study presented in this paper, which uses spaceborne SAR imagery of the North Atlantic, shows that at X and C band at intermediate incidence angles the RAR MTF can be very sensitive to the local wind speed and direction relative to the wave propagation direction, while at L band it is less sensitive. This is in accordance with previous findings by *Brüning et al.* [1994], *Jacobsen and Høgda* [1994], and *Zurk and Plant* [1996]. In X- and C-band SAR images a shift in wind speed and direction as encountered across atmospheric fronts can thus cause, for waves that travel near the range direction, considerable shifts in the apparent wave propagation direction. Another result of our analysis is that at X and C band the RAR MTF for different wave systems is affected differently by a change in wind speed and direction. One wave system may experience a rotation upon imaging while the other does not.

The results obtained in this investigation suggest that an algorithm designed to invert X- and C-band image spectra into ocean wave spectra can yield erroneous results when the dependence of the RAR MTF on local wind speed and direction is not taken into account. The knowledge of the local wind speed and direction is of particular importance when the inversion algorithm is applied to ocean waves that travel close to the range direction and that are imaged at intermediate incidence angles. It is therefore essential to have a good knowledge of the exact local wind conditions in order to retrieve information on the ocean wave spectrum from X- or C-band SAR image spectra.

Acknowledgments. We are indebted to C. Brüning for making available to us his Monte Carlo simulation program. We thank the two anonymous reviewers for their valuable comments. This work has been supported by the German Space Agency (DARA) under the contracts 01QS9016/50QS90165 and 50EE9413.

References

Alpers, W., Monte-Carlo simulations for studying the relationship between ocean wave and synthetic aperture radar image spectra, *J. Geophys. Res., 88,* 1745-1759, 1983.

Alpers, W., D. B. Ross, and C. L. Rufenach, On the detectability of ocean surface waves by real and synthetic aperture radar, *J. Geophys. Res., 86,* 6481-6498, 1981.

Brüning, C., W. Alpers, and K. Hasselmann, Monte-Carlo simulation studies of the nonlinear image of a two-dimensional surface wave field by a synthetic aperture radar, *Int. J. Remote Sens., 11,* 1695-1727, 1990.

Brüning, C., R. Schmidt, and W. Alpers, Estimation of the ocean wave–radar modulation transfer function from synthetic aperture radar imagery, *J. Geophys. Res., 99,* 9803–9816, 1994.

Feindt, F., J. Schröter, and W. Alpers, Measurement of the ocean wave radar modulation transfer function at 35 GHz from a sea-based platform in the North Sea, *J. Geophys. Res., 91,* 9701–9708, 1986.

Hara, T., and W. J. Plant, Hydrodynamic modulation of short wind-wave spectra by long waves and its measurement using microwave backscatter, *J. Geophys. Res., 99,* 9767-9784, 1994.

Hasselmann, K., and S. Hasselmann, On the nonlinear mapping of an ocean wave spectrum into a synthetic aperture radar image spectrum and its inversion, *J. Geophys. Res., 96,* 10713–10729, 1991.

Hasselmann, S., C. Brüning, K. Hasselmann, and P. Heimbach, An improved algorithm for the retrieval of ocean wave spectra from synthetic aperture radar image spectra, *J. Geophys. Res., 101,* 16615-16629, 1996.

Jacobsen, S., and K. A. Høgda, Estimation of the real aperture radar modulation transfer function directly from synthetic aperture radar ocean wave image spectra without a priori knowledge of the ocean wave height spectrum, *J. Geophys. Res., 99,* 14291-14302, 1994.

Kudryavtsev, V. N., C. Mastenbroek, V. K. Makin, Modulation of short waves via the atmospheric boundary layer: A feed-back mechanism, *Boundary Layer Meteorol., 83,* 99-116, 1997.

Melsheimer, C., W. Alpers, and M. Gade, Investigation of multifrequency/multipolarization radar signatures of rain cells over the ocean using SIR-C/X-SAR data, *J. Geophys. Res.,* this issue.

Monaldo, F. M., T. G. Gerling, and D. G. Tilley, Comparison of SIR-B SAR wave image spectra with wave model predictions: Implications on the SAR modulation transfer function, *IEEE Trans. Geosci. Remote Sens., 31,* 1199-1209, 1993.

Plant, W. J., W. C. Keller, and A. Cross, Parametric dependence of ocean wave–radar modulation transfer functions, *J. Geophys. Res., 88,* 9747–9756, 1983.

Romeiser, R., A. Schmidt, and W. Alpers, A three-scale composite surface model for the ocean wave-radar modulation transfer function, *J. Geophys. Res., 99,* 9785–9803, 1994.

Schmidt, A., V. Wismann, R. Romeiser, and W. Alpers, Simultaneous measurements of the ocean wave-radar modulation transfer function at L, C, and X band from the research platform Nordsee, *J. Geophys. Res., 100,* 8815-8827, 1995.

Schröter, J., F. Feindt, W. Alpers, and W. C. Keller, Measurement of the ocean wave–radar modulation transfer function at 4.3 GHz, *J. Geophys. Res., 91,* 923–932, 1986.

Stoffelen, A., and D. L. T. Anderson, Scatterometer data interpretation: Extraction and validation of the transform function CMOD4, *J. Geophys. Res., 102,* 5767-5780, 1997.

Wave Model Development and Implementation (WAMDI) Group, The WAM model: A third generation ocean wave prediction model, *J. Phys. Oceanogr., 18,* 1775-1810, 1988.

Zurk, L. M., and W. J. Plant, Comparison of actual and simulated synthetic aperture radar image spectra of ocean waves, *J. Geophys. Res., 101,* 8913-8931, 1996.

W. Alpers and C. Melsheimer, Institut für Meereskunde, Universität Hamburg, Troplowitzstr. 7, 22529 Hamburg, Germany. (e-mail: alpers@ifm.uni-hamburg.de; melsheim@ifm.uni-hamburg.de)

M. Bao, Centre for Remote Imaging, Sensing and Processing (CRISP), Faculty of Science, National University of Singapore, Lower Kent Ridge Road, Singapore 119260. (e-mail: crsbaomq@leonis.nus.edu.sg)

(Received February 4, 1997; revised January 30, 1998; accepted February 4, 1998.)